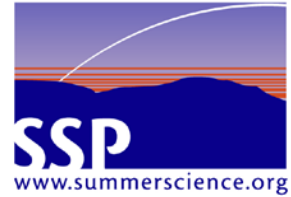# THE SUMMER SCIENCE PROGRAM

SSP
www.summerscience.org

August, 2018

To Whom It May Concern:

This letter is to confirm that **Rishi Sreekanth** of Hockessin, DE, a student at Sanford School, together with his two teammates, successfully completed a research project at the 2018 Summer Science Program at New Mexico Institute of Technology. Rishi operated a research-grade telescope to take images of a near-earth asteroid, then calculated its orbital path, including the chance it will impact Earth in the future.

SSP is one of the oldest (since 1959) and most prestigious pre-college STEM research programs. Rishi was one of 108 students admitted from a pool of 1,157 applicants from around the world, all showing extraordinarily high aptitude and interest in STEM.

SSP immerses these gifted students in a challenging, rigorous, yet supportive environment that requires collaboration and stimulates personal growth. Supported by fast-paced lectures from college professors in calculus-based physics, astronomy, and programming in Python, and hands-on experience with research-grade equipment and software, each participant comes to understand the joys, hard work, frustrations, and ambiguity of authentic scientific research. Each participant is engaged in research-related activities for at least 300 hours over the 39 days and nights.

This intense experience rewards academically gifted teenagers in ways high schools cannot, preparing them to excel at the most selective universities, and to become leaders in their chosen professions.

For more information, visit **summerscience.org** or contact me directly.

Best regards,

Richard D. Bowdon SSP '74
Executive Director, rbowdon@ssp.org

SSP is operated by an independent non-profit 501(c)3 corporation, in cooperation with host campuses New Mexico Institute of Technology, University of Colorado Boulder, and Purdue University, and affiliates California Institute of Technology, Massachusetts Institute of Technology, and Harvey Mudd College.

The Summer Science Program in Astrophysics 2018

Determination of the Orbital Elements of 1627 Ivar (1929 SH) via the Method of Gauss

ABSTRACT

Context. The orbital elements of near-Earth asteroids give us insight into their orientation and projected motion, allowing humanity to understand the potential dangers of these objects. We investigated an asteroid called 1627 Ivar in order to gain information about its orbit and fate.

Aims. After imaging the asteroid over the course of several weeks, we used the Method of Gauss as well as other approaches to analyze our data and determine the orbital elements of 1627 Ivar.

Methods. Using astrometry on our images, we determined the right ascensions and declinations of the asteroid at various times over the span of six weeks. Using these values, we created Method of Gauss codes with additional visualization and statistical features in order to determine the position and velocity vectors, as well as the six orbital elements, of 1627 Ivar.

Results. After calculating our orbital elements, we ran them through statistical analyses and compared them to the values obtained by NASA's Jet Propulsion Laboratory's Horizons Interface. The Monte Carlo method demonstrated the statistical significance of our values. Using our method, we found the following values for the orbital elements:

$$a = 1.853 \text{ AU}$$
$$e = 0.394$$
$$i = 8.4065°$$
$$\Omega = 133.17°$$
$$\omega = 167.765°$$
$$M = 353.5°$$

Conclusions. We found that our values matched those of JPL to around two significant figures, demonstrating that our method was successful. In addition, by working with the Southwest Research Institute, we were able to use our orbital elements to predict via computer simulations that the most likely fate of 1627 Ivar is to crash into the Sun in the distant future.

Determination of the Orbital Elements of 1627 Ivar (1929 SH) via the Method of Gauss

B. Devine, R. Sreekanth, and L. Zeng

The Summer Science Program in Astrophysics
Etscorn Observatory
New Mexico Institute of Mining and Technology
801 Leroy Pl
Socorro, NM 87801

21 July 2018

ABSTRACT

Context. The orbital elements of near-Earth asteroids give us insight into their orientation and projected motion, allowing humanity to understand the potential dangers of these objects. We investigated an asteroid called 1627 Ivar in order to gain information about its orbit and fate.

Aims. After imaging the asteroid over the course of several weeks, we used the Method of Gauss as well as other approaches to analyze our data and determine the orbital elements of 1627 Ivar.

Methods. Using astrometry on our images, we determined the right ascensions and declinations of the asteroid at various times over the span of six weeks. Using these values, we created Method of Gauss codes with additional visualization and statistical features in order to determine the position and velocity vectors, as well as the six orbital elements, of 1627 Ivar.

Results. After calculating our orbital elements, we ran them through statistical analyses and compared them to the values obtained by NASA's Jet Propulsion Laboratory's Horizons Interface. The Monte Carlo method demonstrated the statistical significance of our values. Using our method, we found the following values for the orbital elements:
a = 1.853 AU
e = 0.394
i = 8.4065°
Ω = 133.17°
ω = 167.765°
M = 353.5°

Conclusions. We found that our values matched those of JPL to around two significant figures, demonstrating that our method was successful. In addition, by working with the Southwest Research Institute, we were able to use our orbital elements to predict via computer simulations that the most likely fate of 1627 Ivar is to crash into the Sun in the distant future.

Key words. near-Earth asteroids, 1627 Ivar, orbit determination, orbital elements

1. Introduction

Our goal is to determine the orbit of the near-Earth asteroid 1627 Ivar (1929 SH). More specifically, we are writing code to determine the six orbital elements of the asteroid's orbit. Researching near-Earth asteroids is relevant for determining how close the asteroids are to Earth. Although the probability of humanity's extinction due to asteroid collision seems minimal, only an infinitesimal fraction of the predicted number of asteroids have been discovered. In addition, more asteroid discoveries also have the potential of motivating human space travel; for example, valuable natural resources lacking on Earth could be abundant on an asteroid. While asteroid discoveries are important for reasons of preventing our doom, asteroids could, contrary to popular belief, save humanity in the future as well.

2. Materials and Methods

2.1. Instruments and Software

All of our images were taken using a Celestron C-14 telescope at the Etscorn Observatory in Socorro, New Mexico. We used TheSkyX software to control the telescope, create star charts for finding the asteroid, and locate stars for astrometry and photometry. We used CCDSoft to reduce our images. We processed our data by creating Python programs to perform astrometry, photometry, orbit determination, orbit visualization, and statistical analysis.

2.2. Observations

We were able to go to Etscorn 7 times total, although some nights were clouded out. Before observing, we prepared by finding the ephemeris for a three hour shift centered on the middle of our observing shift, finding a nearby focus star in TheSkyX, and creating a finding chart for the asteroid in TheSkyX. We used the visual filter every time we observed, and primarily used a

60 second exposure time. We took at least 3 sets of 5 images each observing session, spaced out over the course of the observing shift. In addition to raw images of the asteroid, we also took darks with the same exposure times as our lights. Biases had a zero second exposure time. For later reduction of our raw images, we needed biases, darks, and flats with the same filter, which were taken weekly. We generally set the temperature of the CCD chip at -8 degrees Celsius. Our telescope settings generally included a focus of around 4000, 1x1 binning, light frame, and no calibration.

Observation Date (UT)	Conditions	Exp (s)	Filter
06/23/2018 05:00-07:00	Clear	60	V
06/28/2018 03:00-05:00	Clear	60	V
07/02/2018 03:00-05:00	Slightly Cloudy	45	V
07/06/2018 03:00-05:00	Cloudy	N/A	V
07/10/2018 05:00-07:00	Slightly Cloudy	60	V
07/14/2018 03:00-05:00	Cloudy	N/A	V
07/18/2018 05:00-07:00	Clear	60	V

2.3. Calculation Method: Gaussian

The Method of Gauss determines the asteroid's position and velocity vectors iteratively with data from three observations. With data from more observations, the orbit determination becomes more accurate and we can use differential correction to improve our results. In the Method of Gauss, we start by finding an initial value for the range from Earth to the asteroid with the scalar equation of Lagrange. We calculate τ_1, τ_3, and τ from the time intervals between observations in Gaussian days. We can find the directions of the position vectors between Earth and the asteroid, $\hat{\rho}$, from our values of right ascension, α, and declination, δ. We calculate D_o, D_{1j}, D_{2j}, D_{3j} where $j = 1, 2, 3$ by manipulating the $\hat{\rho}$ vectors for each of the observations and the position vector between the Earth and Sun at the time of each observation. With these values, we can solve the scalar equation of Lagrange, an 8th order polynomial, for up to three real positive roots that will be the initial values of r_2, the range to the asteroid, that we iterate. After we have an initial value for r_2, we can use a truncated 2nd order Taylor polynomial for f_i and g_i, where f_1 and g_1 describe the position vector $\boldsymbol{r_i}$. With f and g values, we can use the scalar equations of range to get new values for ρ. Given both the ρ and $\hat{\rho}$ values, we can solve for $\boldsymbol{r}$ and $\dot{\boldsymbol{r}}_2$. Our initial values for and $\boldsymbol{r}$ and $\dot{\boldsymbol{r}}_2$ can then be used in our main iteration. We can now use the expanded Taylor series for f and g to find closer values for $\boldsymbol{r}$ and $\dot{\boldsymbol{r}}_2$, iterating until the difference between the previous value for $\boldsymbol{r}$ and the new value for $\boldsymbol{r}$ is negligible. This gives us our final $\boldsymbol{r}$ and $\dot{\boldsymbol{r}}_2$, which we can use to calculate the orbital elements: semi-major axis (a) , eccentricity (e), orbit inclination (h), longitude of ascending node (Ω), argument of perihelion (ω), and mean anomaly (M).

2.4. Differential Correction

Ideally, the orbital elements that are calculated from the Method of Gauss can be used to backtrack to the same set of right ascensions and declinations. However, this is almost never the case; the calculated right ascension and declination from the calcu-

lated orbital elements will very often differ slightly from the measured right ascension and declination. By using the position and velocity vectors as well as the orbital elements calculated for an observation night, one can optimize the position and velocity vectors. The right ascensions and declinations are needed for the other four observation nights as well; the difference between the observed and calculated right ascensions and declinations will be lowered, and in turn, the root mean squares (RMS) value will also decrease. RMS can be calculated as follows, with n being the number of observation nights times two:

$$RMS = \sqrt{\frac{\sum_1^n(observed - calculated)^2}{n - 6}}$$

Each of the observed minus calculated values, five for right ascension and five for declination, depend not only on the changes for each of the components of $\boldsymbol{r}$ and $\dot{\boldsymbol{r}}$, but also the partial derivatives of the right ascension and declination with respect to that vector component. The partial derivatives will number sixty, since there are five observations and each has a right ascension and declination value. Any one of the sixty will follow this form:

$$\frac{\partial \alpha}{\partial x} = \frac{\alpha(x + \Delta, y, z, \dot{x}, \dot{y}, \dot{z}) - \alpha(x - \Delta, y, z, \dot{x}, \dot{y}, \dot{z})}{2\Delta}$$

Also, Δ is equal to some small amount, in our case 10^{-4} since the partial derivatives are being approximated. For each component, we can sum the partial derivatives from 0 to twice the number of observations. Now we have six summed partial derivatives. A six by one matrix, a, will contain elements that are the sum from 0 to twice the number of observations of the observed minus calculated values times one of the six summed partial derivatives. It will be equal to another matrix, J, in which each element is the product of two of the six partials, which have already been summed. J is multiplied by our unknown matrix, of size (6, 1) in which each element is the change in the value of the respective component. We solve for this matrix with the other two known using the inverse of J.

$$\begin{bmatrix} \Delta x \\ \Delta y \\ \Delta z \\ \Delta \dot{x} \\ \Delta \dot{y} \\ \Delta \dot{z} \end{bmatrix} = J^{-1}a$$

We can now update $\boldsymbol{r}$ and $\dot{\boldsymbol{r}}$ with these changes in components, and calculate new, differentially corrected orbital elements. If the differential correction worked, the RMS would decrease, since the observed and calculated right ascensions and declinations will be closer.

2.5. Monte Carlo

Due to having a time constraint of five weeks and having to share one telescope among 12 teams, we were only able to achieve a handful of successful observations. However, using statistics, we can calculate theoretically infinite sets of orbital elements by generating normal distributions. This is where the Monte Carlo simulations come into play. Our code for astrometry gives us αs and δs, along with error values. From there, we can generate n random normal distributions, which we can plug into our orbit determination code. This will generate n orbital elements centered on a mean, of which we can find the sample mean, $\bar{x}$, and the standard deviation of the sample, s_x. In addition, we can plot the normal distribution as a histogram using Python's matplotlib.pyplot library.

2.6. Jack Knife

The Jack Knife method of measuring uncertainty in orbital elements involves random normal distributions of a particular orbital element. From a list of these ever so slightly different orbital elements, one can iterate through the list, taking away and replacing that element each iteration. One will then have *n* lists of *n - 1* of an orbital elements. One can take the mean of each of these lists, and find the so-called Jack mean of these means. This Jack mean is the best value of the orbital element, and the standard deviation of the jack mean is the uncertainty on that orbital element. However, these standard deviations are inaccurate representations of the uncertainty, since the replacement method employed by Jack Knife causes the standard deviation to plummet far below a reasonable value.

2.7. Orbit Visualization

An extremely helpful tool to help visualize what our orbital elements actually mean is VPython. We can take the orbital elements of our asteroid and Earth as parameters and use rotation matrices to calculate the position vectors of the Earth and Ivar in a while loop to continuously update their position. Our orbit visualization code is capable of displaying the trails of the orbits, the current date, and even has skins to model the appearance of the respective bodies. In addition, the Sun is a light source, and casts light on the orbits and bodies.
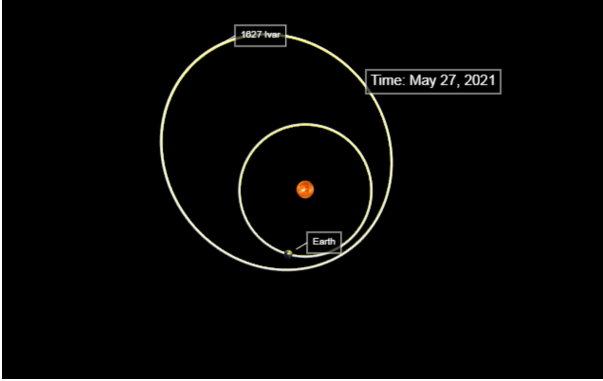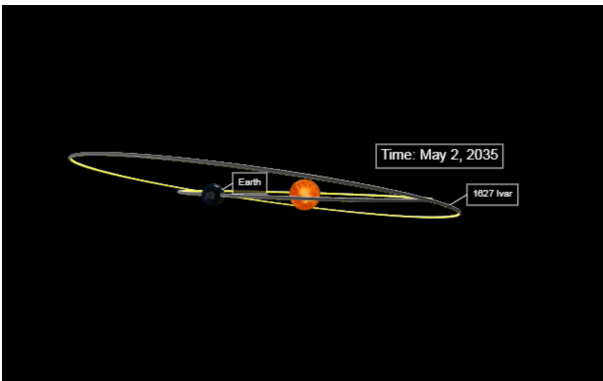

Fig. 1. Overhead View

Fig. 2. Edge-on View

3. Data and Analysis

3.1. Utilization of Data

Through the use of Least Squares Plate Reduction (LSPR) Astrometry and Aperture Photometry, we were able to determine right ascensions and declinations and apparent magnitude and signal-to-noise ratios, respectively, of the asteroid.

3.1.1. Reduction of Data

After each observation night at Etscorn Observatory, we had at least three sets of raw images of our asteroid and its star field,as well as the following calibration images: darks, biases, and flat fields.The flat fields would be taken once per week by a chosen observing team. The calibration images can be, simply put, subtracted from the raw images (flats are technically divided) to get a reduced image. These reduced images can then be aligned to make the positions of the background reference stars equal to one another. This is useful when choosing 4reference stars for an observing night's astrometry and photometry: any of the images from a single night can be used for astrometry or photometry and all use the same reference stars with aligned images.

3.1.2. Least Squares Plate Reduction

From the best reduced and aligned image of each observation night, we had a position of the asteroid on the image (x, y), and our goal was to convert that to an equatorial position on the sky, in the form of right ascension and declination (α, δ). We were able to determine the (x, y) centroided positions of twelve reference stars for each observation night. The reason we centroided the positions was to take into account brighter pixels (i.e. pixels with a larger count). We also used TheSkyX UCAC-3.0 catalog to determine the J2000.0 α and δ for each of those reference stars. We were even able to overlay TheSkyX on the CCDSoft image to accurately find dimmer reference stars and match it up with their αs and δs. Once we have our input file, we can cal-
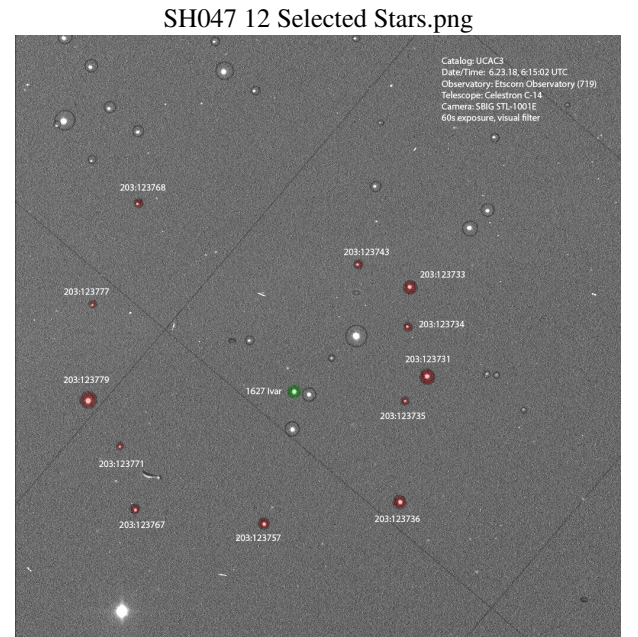

Fig. 3. Photoshop Layover

culate the plate constants and, from those, right ascensions and

declinations. However, we also took into account the fact that there is a limit to how well LSPR works due to the fact that we are transferring from a flat image to spherical positional coordinates. This is why we also flattened and then unflattened our αs and δs to obtain more precise coordinates. Of course, there will always be uncertainties attached to any calculations, and so we also calculated the uncertainties on our coordinates, and they are reported section 3.1. When we calculated the plate constants (b_1, a_{11}, a_{12} for α; b_2, a_{21}, a_{22} for δ), we were simultaneously solving three equations (separately for δ), in matrix form shown below:

$$\begin{bmatrix} \alpha_i \\ \alpha_i x_i \\ \alpha_i y_i \end{bmatrix} = \begin{bmatrix} N & x_i & y_i \\ x_i & x_i^2 & x_i y_i \\ y_i & x_i y_i & y_i^2 \end{bmatrix} \begin{bmatrix} b_1 \\ a_{11} \\ a_{12} \end{bmatrix}$$

Thus, when we were calculating the uncertainty on α (or δ), we lose three degrees of freedom (three simultaneous equations), and the uncertainty on α (or δ) is:

$$\sigma_\alpha = \sqrt{\frac{1}{N-3} \sum_1^N (\alpha_{actual} - \alpha_{fit})^2}$$

Where N is the number of reference stars, twelve; α_{actual} is TheSkyX α; and α_{fit} is the asteroid's α after running through the LSPR code. The process can be repeated for δ, and these uncertainties are reported in section 3.1.

3.1.3. Aperture Photometry

The purpose of completing photometry was to determine the signal-to-noise ratio and apparent magnitude (m) of our asteroid. We had two methods of calculating m; both used a circular aperture and took into account fractional pixels. The first method looped through individual pixels 0.01 at a time and determined if the sub-pixel was inside the aperture radius. If so, it was added to a count for that pixel. Once the code finished looping through one pixel, we would be able to calculate the area percentage of the pixel inside the aperture radius, and multiply this amount by that pixel's count. Doing this for all pixels in a square matrix around the circular aperture, we could bypass using a circular aperture. However, we also had a second method of completing aperture photometry that used Python's SciPy library and double integrals. We defined a method of determining the specific area of a pixel given its x,y coordinates and the radius of the circle. We chose to use double integrals as they were far more efficient at completing this task than regular integrals. We also determined that the double integral method was more accurate at determining an m for our asteroid, and so we used those magnitudes for our Minor Planet Center Report and in second table in section 3.1. We were also able to determine the instrumental magnitude uncertainty for the reference stars and asteroid using the following:

$$\sigma_m = \frac{1.0857}{SNR}$$

We could also construct a graph of each of TheSkyX apparent magnitudes versus the $\log_{10}(Signal)$ of each of the stars. The y-intercept of this graph can be added to the instrumental magnitude of our asteroid to calculate the apparent magnitude of our asteroid.

$$m_{apparent} = -2.5 \log_{10}(Signal) + b,$$

with

$$m_{instrumental} = -2.5 \log_{10}(Signal)$$

3.2. Orbital Elements Descriptions

3.2.1. Semi-major Axis (a)

The semi-major axis defines the size of the elliptical orbit. The semi-major axis is equal to half of the major axis of orbit.

$$a = \left(\frac{2}{|\boldsymbol{r}|} - \dot{\boldsymbol{r}_2}\right)^{-1}$$

3.2.2. Eccentricity (e)

The eccentricity describes the shape and flatness of the orbit. It can be calculated once we know the value of a.

3.2.3. Orbit Inclination (i)

The orbit inclination gives the angle at which the orbit is tilted with respect to the ecliptic plane. Since we know $\boldsymbol{r}$ and $\dot{\boldsymbol{r}_2}$, we can determine i.

3.2.4. Longitude of Ascending Node (Ω)

The longitude of the ascending node helps place the asteroid's orbital plane with respect to our orbital plane. With the longitude of ascending node, we must be careful to not introduce quadrant ambiguities. We can find Ω once we know i.

3.2.5. Argument of Perihelion (ω)

The argument of perihelion is the distance from the ascending node to perihelion. It orients the object's orbit within its orbital plane. We can use the true anomaly– distance from perihelion to the asteroid– and the angular distance from the ascending node to the asteroid to calculate ω.

3.2.6. Mean Anomaly (M)

The mean anomaly places the asteroid in a specific spot along its orbit.

3.3. Tables of Orbital Elements

Refer to *Tables Appendix*, Section 1

3.4. Results of Differential Correction

Refer to *Tables Appendix*, Section 2 For all permutations of observation nights, the orbital elements change extremely little after differential correction. Although it may seem difficult at first to assess whether the differential correction helped with such little change, an RMS value is calculated before and after the correction. This value should decrease after correction, since the observed minus calculated value should have been reduced. This was the case for all permutations, which means that the differential correction assisted in improving the orbital elements.

3.5. Results of Monte Carlo

Performing Monte Carlo simulations, we are able to obtain histograms for our orbital elements (Fig.4.)

We can repeat the Monte Carlo process for all permutations of our data set. For example, five observations will yield permutations of $\{1, 2, 5\}$, $\{1, 3, 5\}$, and $\{1, 4, 5\}$, keeping the first and
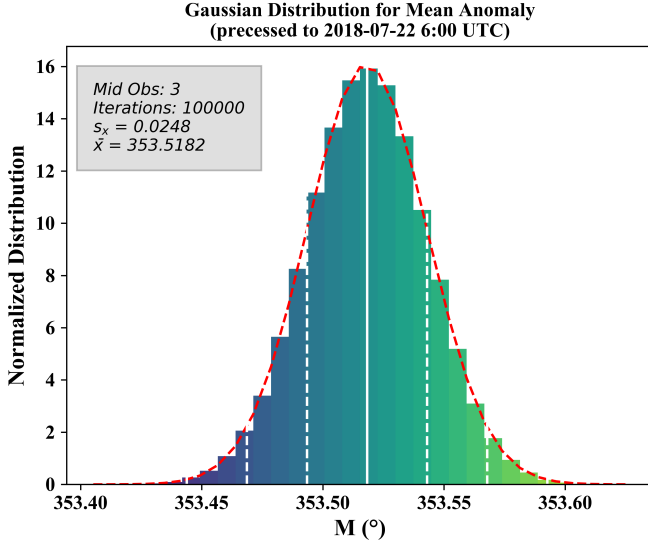
Fig. 4. Normal Distribution (for the mean anomaly) using observations 1,3,and 5.

Fig. 6. The Gaussian distribution for our trimodal distributions (for mean anomaly). The s_x represents our average standard deviation for our observations, and the $\bar{x}$ represents our our sample mean. (*this is shown as the dashed red line in Fig.5.)

last observations constant to maximize the time span of our data. After we have run each permutation of our observations for all six orbital elements, we can graph the three sets together. This produces a trimodal distribution (Fig.5.), which is possibly due to our errors for astrometry being surprisingly low, especially for our αs, therefore causing our normal distributions for each of our permutations to have a very low s_x (Fig.4.).

by taking its normal distribution, we believe we are achieving a more representative sample of our data since we are averaging our permutations.

3.6. Results of Jack Knife

The graph below shows the distribution of Jack Means, as well a vertical line for the final Jack Average, for that orbital element. The standard deviation is not shown; since the Jack Knife method involves removing one value from the list of a single orbital element each iteration, the uncertainty tends to plummet. However, the jack average should be extremely close to the mean obtained from the Monte Carlo method, as it was for us. In the *Tables Appendix*, Section 4, a table of Jack Averages for each orbital element can be seen.

Fig. 5. Trimodal distribution (of mean anomalies) comprised of the three permutations with a normal distribution fit.

Ideally, all three distributions should overlay perfectly, and it is a bit odd that they are several σ apart. This could be caused be some unforeseen error that was unaccounted for when making our normal sample of αs and δs. As an alternative to graphing our histograms separately, we can combine the each set of orbital elements into a singular list and find the normal distribution of that list (Fig.6.).

This produces a much higher (and more reasonable) s_x relative to the s_xs of our individual normal distributions. In addition, since we are not just relying on one set of data, our $\bar{x}$ is slightly closer to the orbital elements listed by JPL and MPC. While we are unsure of the causes of our trimodal distribution,
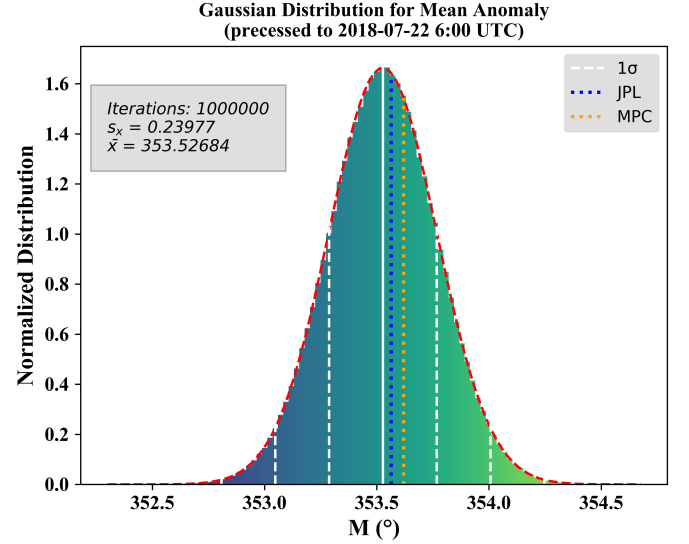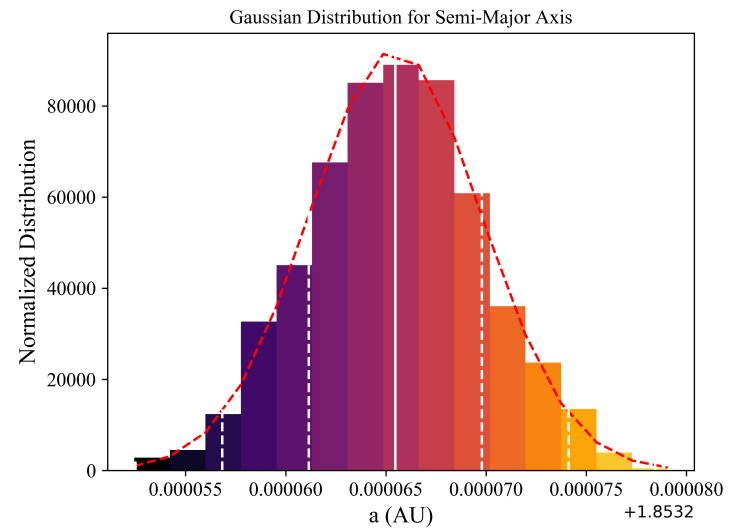

Fig. 7. Distribution of Jack Means of Semi-Major-Axis

3.7. Asteroid Family

Based on our orbital elements, 1627 Ivar belongs to the Amor family of asteroids. An asteroid is classified as Amor if its semimajor axis (a) is greater than 1.0 AU and its perihelion distance (q)is higher than Earth's highest point (aphelion = 1.017 AU) and lower than 1.3 AU. Our orbital elements find that Ivar satisfies these requirements, with $a = 1.853$ and $q = 1.125$.

3.7.1. 1627 Ivar History

Ivar was named after Ivar Hertzsprung, the late brother of its discoverer. Ivar has a diameter between 8.37 and 10.2 km and is non-spherical. Ivar is classified as a stony S-type asteroid and has a spectral type that indicates a siliceous composition.

3.8. Comparison of Results

Our results agree with the other team's predicted asteroid position. The other team studying 1627 Ivar measured right ascension = 14h 47m 41.82s and declination = 05° 42' 33.83" for their middle observation. Our ephemeris generator predicted right ascension = 14h 47m 41.72s and declination = 05° 42' 45.76" for their middle observation. Therefore, our results agree with the other team's predicted position.

3.9. Orbit Integration and Asteroid Fate Predictions

Working with the Southwest Research Institute (SWRI), we could perform long-term integrations to determine changes in 1627 Ivar's orbit and its eventual fate using our calculated orbital elements. While seeing the probability distribution of where our asteroid will end up is interesting, it also can prove essential to our survival if we determine a high probability of hitting Earth in the relatively near future. Through observation, we found asteroid values for r and $\dot{r}$. We integrated the orbits of several asteroid "particles" with slight perturbations of 10^{-5} of the position or velocity vector components. These offsets can be done by hand or by a Python random generation script. We then run simulations using the Swift software and analyze the statistical data to determine the fate of our asteroid. This was a 50 million year simulation, but since we ran many of these simulations on different computers, not all had time to finish. The average time for the 8 simulations we did was 32.214 million years. Each simulation started with 20 asteroid particles. We started thus with 160 particles; 50 completely survived the simulation, and thus our asteroid had a 31.25% chance of surviving the simulation. Of those that did not survive, which were 110 particles, in the *Tables Appendix*, Section 5, is a table of the different fates, the number of particles that succumbed to that fate, and the probability of 1627 Ivar succumbing to a particular fate during this time period (32.214 million years). The most likely fate of 1627 Ivar is that its perihelion becomes too small and it gets too close to the Sun.
Refer to *Tables Appendix*, Section 5.

4. Conclusion

We found that our orbital elements generally matched those of JPL Horizons within our uncertainties. Our research confirms the utility of the Method of Gauss with respect to asteroids with small ρ values (in other words, for near-Earth asteroids). Some sources of inherent error stemmed from the imprecision of the equipment we used and imperfections in our data and code. For

future research, we recommend taking many sets of data, using sufficiently long exposure times, and using additional statistical analysis to verify the accuracy of our data.

5. Appendices

5.1. Minor Planet Center Report

COD 719
CON A. W. Rengstorf
CON [adamwr@pnw.edu]
OBS R. Sreekanth, B. Devine, L. Zeng
MEA R. Sreekanth, B. Devine, L. Zeng
TEL 0.36-m f/11 reflector + CCD
NET UCAC-3.0
BND V
NUM 6
ACK Team 9 - 1929 SH
01627 C2018 06 23.23631 14 36 38.97 +11 20 38.3 12.5 V 719
01627 C2018 06 23.24985 14 36 39.10 +11 20 24.4 12.3 V 719
01627 C2018 07 10.24863 14:50:17.94 +04:44:53.9 12.3 V 719
01627 C2018 07 10.26043 14:50:18.82 +04:44:33.0 12.4 V 719
01627 C2018 07 18.22600 15:03:24.30 +00 29 34.9 12.6 V 719
01627 C2018 07 18.24871 15 03 26.80 +00 28 47.8 12.5 V 719

5.2. Cloudy Night Experiments

5.2.1. Data Collection Strategy

During clouded out observation sessions from July 5, 2018 through July 17, 2018, we performed cloudy night experiments designed to investigate the effects of changing different variables on darks and biases. We took a series of darks at different exposure times and temperatures, and Data was collected using a 14" Celestron C-14 at Etscorn Observatory. Temperature was adjusted using the temperature setup, and exposure times were changed using the "Take Series" feature.

5.2.2. Methodology

In order to analyze and process the data, we created programs in Python.

- All data had 20 pixels trimmed off the edges in order to avoid edge effects
- Signal was found using average values of all pixel counts
- Noise (uncertainty of signal) was found by creating noise images and averaging
  - Between two arrays, σ values for each pixel were calculated using

$$\sigma = \frac{|x_2 - x_1|}{\sqrt{2}}$$

  - The uncertainty for two arrays was the average sigma value for every pixel
- The darks were first reduced in CCDSoft with biases taken at the same temperature
- The calculated uncertainties reflect the variation of a pixel from one image to the next
- Exponential best fit lines were generated with scipy.optimize curve fit
- Uncertainty of slope was calculated with linear regression (scipy.stats.linregress). The coefficient of determination equals r^2, where r is the correlation coefficient.

5.2.3. Expected Results Given Initial Assumptions

– Dark current increase linearly with exposure time
– Dark-count rate depends on temperature in a relation that agrees with the Arrhenius law
– Bias frames do not depend on temperature

We assume that dark current is affected by exposure time and by the temperature, but that bias frames do not depend on temperature.

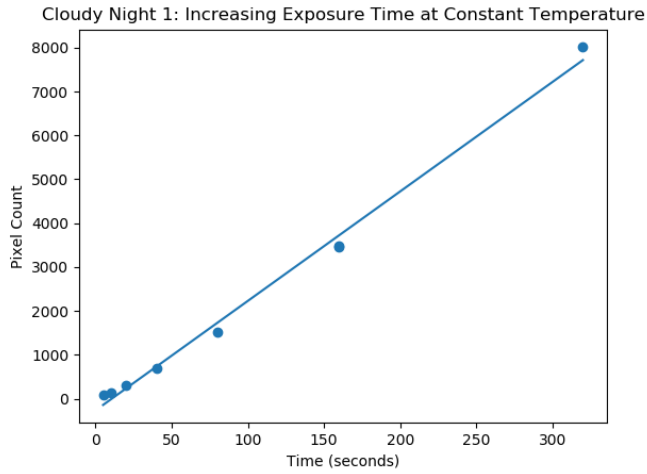### 5.2.4. Cloudy Night 1: Dark Current Characterization

Fig. 8. Plot: pixel count vs time at constant temperature for darks
line of best fit: $y = mx + b$
m = 24.95058354937219
b = -267.0498589155554
r^2 = 0.9935295225214038

The linear best fit line fits data points closely. Based on simple visual inspection, there is no obvious curve to the data. For other curves, an exponential curve may better fit the data.
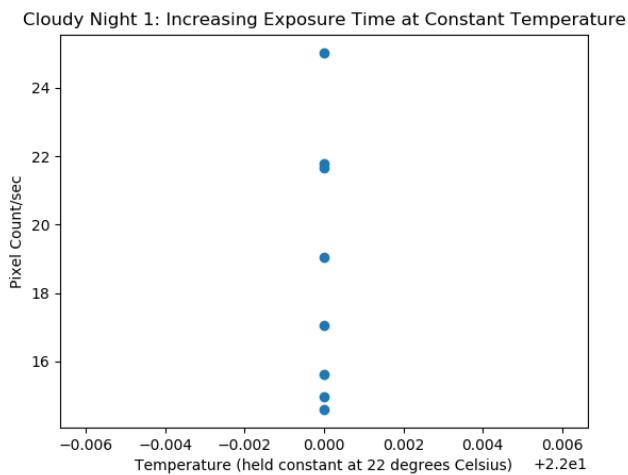
Fig. 9. Plot: pixel count/sec vs temperature for darks

Figure 2 shows increasing exposure time at a constant temperature. Since all of the darks were taken at a constant temperature, the graph shows a straight vertical line. The points near

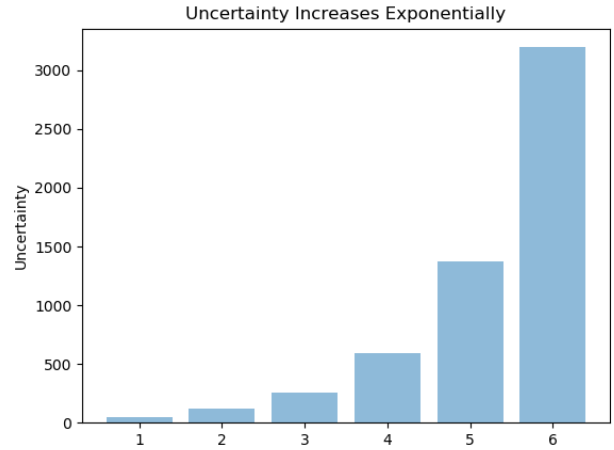the lower pixel count/second values are closer together than the points with higher pixel count/second values.

Fig. 10. Uncertainty of Signal (Noise)

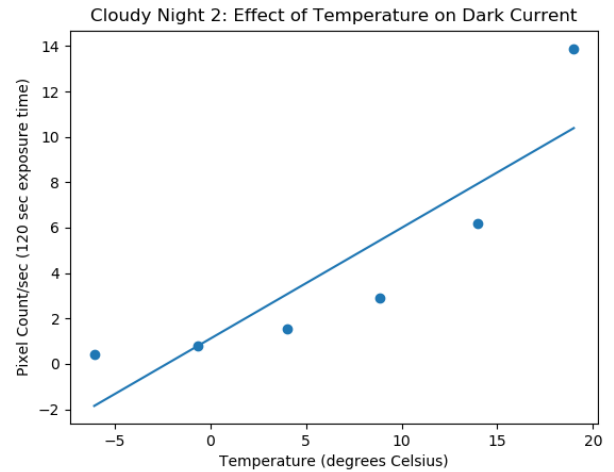### 5.2.5. Cloudy Night 2: Dark Current Characterization

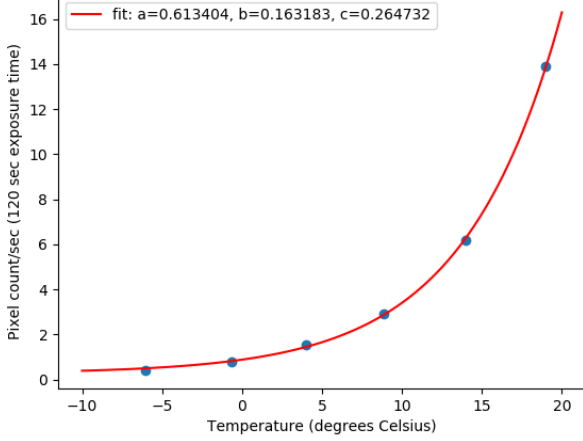**Fig. 11.** Plot: pixel count/sec vs temperature for darks: linear fit

Through simple visual inspection, a straight line of best fit would not fit the data well. There is an obvious exponential curve to the trend, and an exponential function better fits the data.

The dark current fits with the Arrhenius law because the slope of 1/temperature and log10(pixel count) is linear. The exponential prefactor is the y intercept, given by the line as approximately 19. The slope of the line is -4715 ; the activation energy (in the same units as the Boltzmann constant times the temperature) multiplied by the universal gas constant is equal to the slope. The activation energy can be estimated to be approximately -40,000 m^2kgs^{-2}.
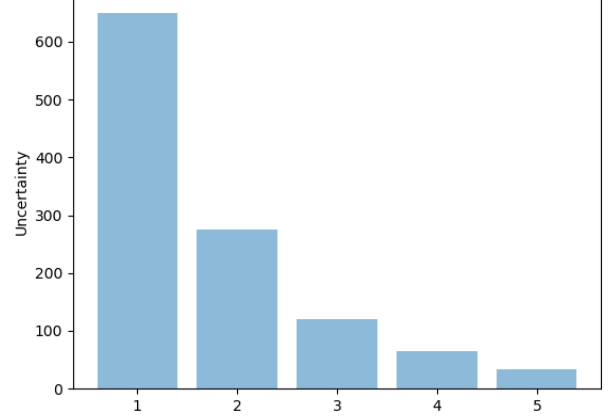
5.2.6. Cloudy Night 3: Bias Level Characterization

The hypothesis is that bias frames do not depend on temperature. If biases are temperature independent, the slope will be closer to 0 than the uncertainty on the slope.
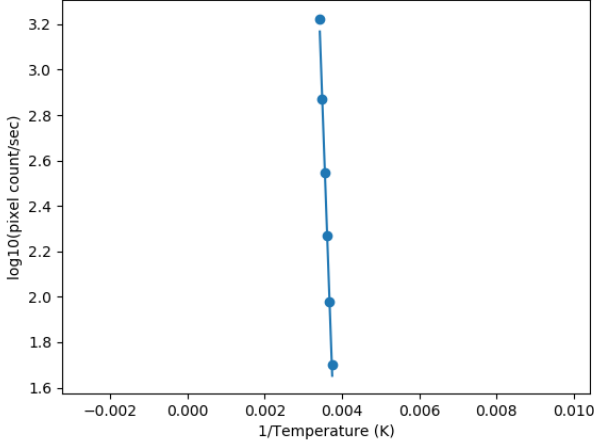
Fig. 12. Plot: pixel count/sec vs temperature for darks: exponential fit

Fig. 14. Uncertainty of Signal (Noise)

Fig. 13. Plot: 1/temperature vs log10(pixel count/sec) for darks (Arrhenius law)

$$\text{line of best fit: } y = mx + b$$
$$m = -4714.672353338777$$
$$b = 19.314217466509643$$
$$r^2 = 0.9944974700654616$$
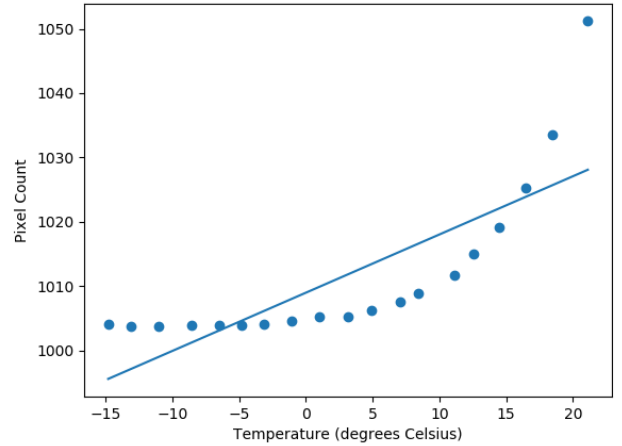
Fig. 15. Plot: pixel count vs temperature for biases: linear fit

$$\text{line of best fit: } y = mx + b$$
$$m = 0.9054343814416396$$
$$b = 1008.9583427059991$$
$$r^2 = 0.6244069630029595$$

The linear line of best fit for bias levels is a moderately poor fit for the data, which clearly would be modeled better by an exponential function. The dark current fits with the Arrhenius law because the slope of 1/temperature and log10(pixel count) is linear. The exponential prefactor is the y intercept, given by the line as 19.3. The slope of the line is -4715 ; the activation energy (in the same units as the Boltzmann constant times the temperature) multiplied by the universal gas constant is equal to the slope. The activation energy can be approximated as -4000 $m^2 kg s^{-2}$.

5.2.7. Discussion

Most of our initial assumptions were justified according to the data we collected. However, our data does not confirm the hypothesis that biases are temperature independent. For the biases (Cloudy Night 3), there was a non-zero slope fit to the line, but the line was clearly exponential as well. Since the slope

was not closer to zero than the uncertainty on the slope is, it is not safe to conclude that biases are temperature independent. For the darks, the data collected with a warmer CCD chip had more dark current. Intuitively, this makes sense because dark frames contain hot pixels, thermal signal and random noise. The darks taken with a longer exposure time had more dark current as well. Since we waited for the CCD chip temperature to stabilize in between collecting data sets, our temperature regulation was stable to within 0.5 degrees, with moderately little variation affecting our overall results.
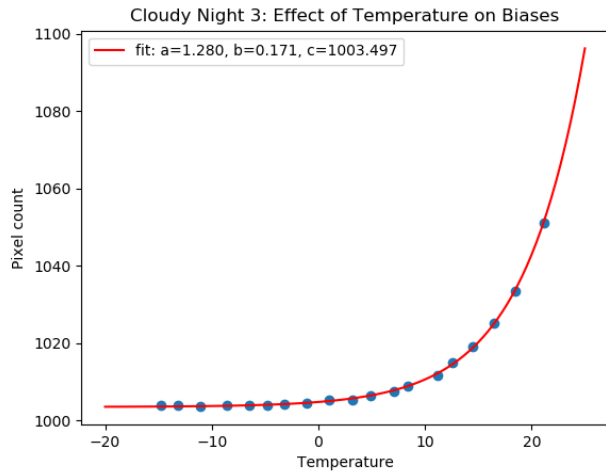
Fig. 16. Plot: pixel count vs temperature for biases: exponential fit
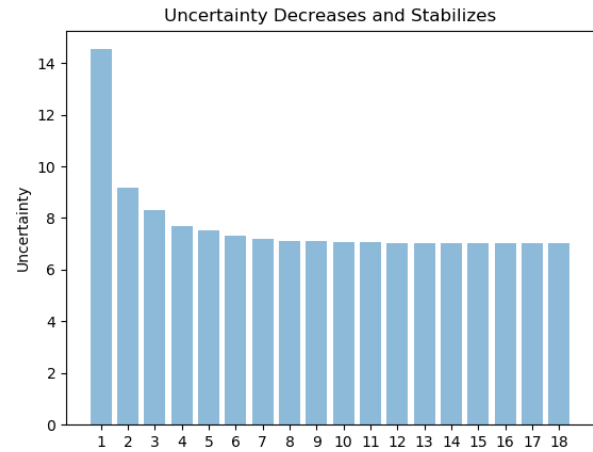

Fig. 17. Uncertainty of Signal (Noise)

References

[2015] Southwest Research Institute, Orbit Integration Packet, Summer Science Program
[2017] A. Rengstorf, Orbit Determination Packet, Summer Science Program

Tables Appendix

B. Devine, R. Sreekanth, L. Zeng

21 July 2018

1 Preliminary Data

1.1 Right Ascensions and Declinations

Observation (UT)	α	δ
2018 06 23 05:40:17	14h 36m 38.97s	+11° 20' 38.30"
2018 06 28 03:46:04	14h 38m 42.96s	+09° 47' 28.43"
2018 07 02 03:33:36	14h 41m 29.81s	+08° 19' 02.62"
2018 07 10 06:00:11	14h 50m 18.06s	+04° 44' 51.42"
2018 07 18 05:58:08	15h 03m 26.80s	+00° 28' 47.83"

1.2 Uncertainties, Apparent Magnitudes, and SNR

σ_α (")	σ_δ (")	m	SNR
±0.04	±0.45	12.5	179.8
±0.03	±0.34	12.1	208.8
±0.03	±0.47	12.4	155.4
±0.01	±0.39	12.3	107.9
±0.03	±0.23	12.5	134.9

2 Tables of Orbital Elements

2.1 Orbital Elements

Mean anomaly has been precessed to July 22,2018 06:00 UT.

Team Member	a (AU)	e	i (°)	Ω (°)	ω (°)	M (°)
B. Devine	1.853	0.394	8.4045	133.1764	167.76583	353.5182
R. Sreekanth	1.853	0.393	8.4065	133.1730	167.76478	353.5214
L. Zeng	1.853	0.394	8.4065	133.1729	167.7647	345.01

2.2 Orbital Elements: Uncertainties

Team Member	a (AU)	e	i (°)	Ω (°)	ω (°)	M (°)
B. Devine	0.00447	0.00124	0.01676	0.02827	0.00422	0.02535
R. Sreekanth	0.00427	0.00123	0.00028	0.00049	6.9431×10^{-5}	0.00042
L. Zeng	0.00450	0.00127	0.01600	0.02719	0.00411	0.02668

3   Differential Correction Tables

Mid Obs = 2	Before	After
a (AU)	1.8025	1.8026
e	0.37887	0.37888
i (°)	8.2007	8.2033
Ω (°)	133.5174	133.5453
ω (°)	167.80208	167.76519
M (°)	353.2444	353.2494
RMS	8.23×10^{-4}	7.41×10^{-4}
Mid Obs = 3	Before	After
a (AU)	1.8534	1.8536
e	0.39378	0.39380
i (°)	8.4065	8.4094
Ω (°)	133.1730	133.2019
ω (°)	167.76480	167.72735
M (°)	353.5214	353.5262
RMS	8.10×10^{-4}	7.12×10^{-4}
Mid Obs = 4	Before	After
a (AU)	1.9110	1.9112
e	0.40973	0.40975
i (°)	8.6238	8.6273
Ω (°)	132.8138	132.8438
ω (°)	167.69552	167.65849
M (°)	353.81842	353.82249
RMS	7.96×10^{-4}	6.73×10^{-4}

The orbital elements before and after differential correction has been performed, as well as the root mean square (RMS) value before and after. The RMS has decreased in all three cases, showing that differential correction was successful.

4 Jack Averages

This table shows the Jack Average of each orbital element. It should be extremely close to the actual measured value of the orbital element.

Orbital Element	Jack Average
a (AU)	1.853
e	0.3937
i (°)	8.4064
Ω (°)	133.173
ω (°)	167.7648
M (°)	353.5212

5 Probabilities of Different Fates of 1627 Ivar

The total number of particles here is 110. The original total was 160, but 50 survived the simulation. This table shows probabilities of particles that did not survive the simulation.

Fate	Number of Particles	Probability (%)
Too close to Sun	81	73.64
Ejected from Solar System	14	12.73
Too close to Earth	7	6.36
Too close to Venus	5	4.55
Too close to Mars	1	0.91
Too close to Jupiter	1	0.91
No convergence	1	0.91
Too close to Saturn	0	0.00